Research Article Vol. 32, No. 22 / 21 Oct 2024 / *Optics Express* 39469

Optics EXPRESS

Ultrafast diffraction algorithms for light-in-flight holography

David Blinder[1,2,3,*] **and Takashi Kakue**[3]

[1] *Department of Electronics and Informatics (ETRO), Vrije Universiteit Brussel (VUB), Pleinlaan 2, B-1050 Brussels, Belgium*
[2] *IMEC, Kapeldreef 75, B-3001 Leuven, Belgium*
[3] *Graduate School of Engineering, Chiba University, 1-33 Yayoi-cho, Inage-ku, Chiba-shi, Chiba, Japan*
[*] *david.blinder@vub.be*

Abstract: Digital light-in-flight (LIF) holography is an ultrafast imaging technique capable of single-shot simultaneous 3D and femtosecond time resolution acquisitions of light pulse propagation. However, the numerical diffraction algorithms used to model light on femtosecond timescales are currently limited in scope, accuracy, and efficiency. We derive an analytical model capable of modeling LIF hologram formation for various optical setup configurations, able to model 3D objects and precisely account for the limited temporal coherence of the signal. We design an efficient algorithmic implementation and validate the system in numerical simulations and with an experimental LIF holographic recording setup. We report ultrafast numerical diffraction over 10,000 times faster than the reference technique, with higher accuracy and capable of modeling 3D samples, thereby broadening its application domain.

1. Introduction

Real-time imaging of high-speed phenomena has brought significant advances across scientific fields, allowing for modeling transient phenomena in physics, chemistry, and biology [1]. Mainly, ultrafast phenomena in the range of picoseconds down to femtoseconds are essential to study [2], such as atomic and molecular dynamics [3], material processing using femtosecond laser fabrication [4], light-matter interactions [5] and the generation of laser-induced plasma [6].

The analysis of transient phenomena has been powered by high-speed camera technology, which has made remarkable progress over the past several decades. Recent developments in silicon-based image sensors, such as CMOS, have improved temporal resolutions to up to $\sim 10^7$ frames per second (fps) in commercially available high-speed cameras such as the Kirana7M, Shimadzu HPV-X2, and Phantom TMX-7510. Backside-illuminated multi-collection-gate (BSI MCG) image sensors have achieved experimental imaging speeds of $\sim 10^8$ fps [7]. Yet, capturing light at even ~10 ns per frame means that light will travel about ~3 m over that time, precluding its use in studying ultrafast dynamics, especially in microscopic objects.

Further increasing the framerate has been achieved with specialized illumination and post-processing techniques. This has primarily been facilitated by ultrashort pulsed lasers, such as in optical polarigraphy [8] and in stimulated Raman microscopy [9]. Moreover, the temporal resolution can be further increased with, e.g., spectral encoding, streak cameras, and computational techniques such as compressed sensing [10,11].

However, many ultrafast phenomena are nonrepeatable or challenging to reproduce, requiring single-shot imaging. This eliminates many ultrafast imaging techniques relying on laser pulse trains. Moreover, many applications require the acquisition of three-dimensional (3D) information. That is why we mainly focus on light-in-flight (LIF) holography. The core idea of recording the time coherence of pulsed lasers was pioneered by Staselko et. al. [12], followed by Abramson being the first to propose optical light-in-flight holography [13]. It has enabled the sectioning and visualization of various 3D objects [14] and flows [15]. The advent of CCD and CMOS

#538935 https://doi.org/10.1364/OE.538935
Journal © 2024 Received 7 Aug 2024; revised 3 Oct 2024; accepted 4 Oct 2024; published 15 Oct 2024

sensors and powerful computers has enabled the use of digital LIF holography [16,17], bringing all the benefits of conventional digital holography w.r.t. its analog counterpart. This technique achieves one of the highest temporal resolutions with a single laser pulse, exceeding 10^{13} fps [1].

1.1. Digital LIF holography

The principle of LIF holography is shown in Fig. 1(a). It can be viewed as an extension of conventional holography, with the main difference being that the light source is an ultrashort pulsed laser rather than a continuous one. The emitted pulse is split into a reference pulse and an object pulse; each widened by a beam expander. The reference pulse will directly illuminate the recording material or device (i.e., digital camera sensor), while the object pulse will illuminate the object to be recorded. In this diagram, the object is illuminated in transmission mode, which is often preferred for transparent samples. Generally, the transparent object is a scattering medium or has light scattering properties. The low temporal coherence of the laser pulse can be leveraged to extract temporal information since interference fringes form only when light from the two arms arrives (nearly) simultaneously at the recording device.

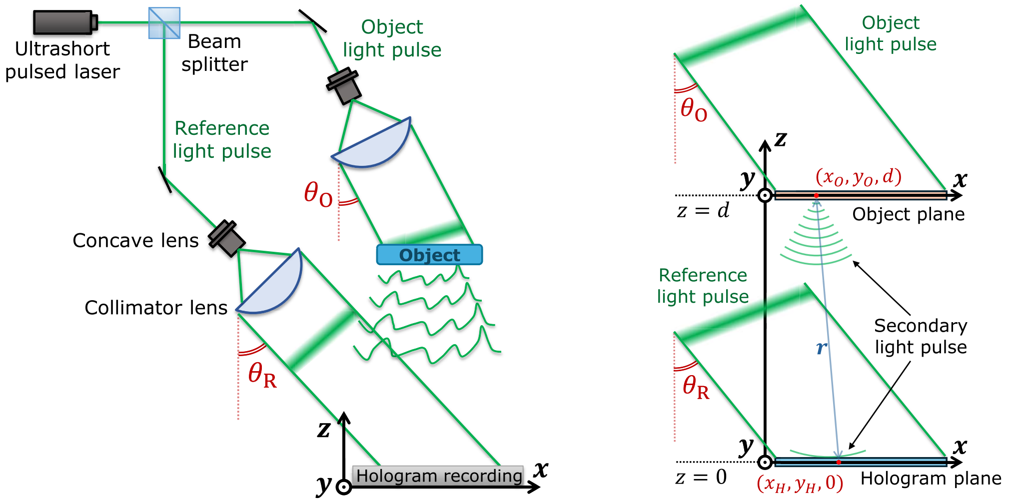

(a) Setup configuration

(b) Setup geometry

Fig. 1. Diagrams of digital LIF holography. (a) The setup schematic shows the main optical setup components; (b) an illustration of the setup geometry with notational conventions.

A second significant difference is the oblique incidence angles for reference and object pulses, denoted θ_R and θ_O in Fig. 1, respectively. This will cause the light pulses to progressively reach the object and hologram planes in the lateral direction, shown to arrive from left to right along x in Fig. 1. It results in a (near-)linear relationship between the incidence time and the lateral direction of the recording material. After recording, the hologram signal can be processed by extracting sub-holograms with a limited width along the x-axis. As the time is related to the x-position of the window, a video can be generated by progressively reconstructing sub-holograms into video frames for linearly increasing x positions of the window center.

The conditions for interference are illustrated in Fig. 1(b); the contribution of an object point with coordinates (x_O, y_O, d) emitting a secondary light pulse will only meaningfully interfere with the reference pulse if it satisfies [18]:

$$|x_H \sin\theta_R - x_O \sin\theta_O + d - r| \lesssim cW_{\mathrm{th}} \quad \text{where} \quad r = \sqrt{(x_H - x_D)^2 + (y_H - y_D)^2 + d^2}. \tag{1}$$

c is the speed of light in vacuum, and W_{th} is the temporal length of the pulse, typically characterized by its full width at half maximum (FWHM). Note that Eq. (1) is not very rigorous; we will derive a more precise expression in the following sections.

Digital LIF holography can fully reconstruct the wavefield of light, encoding 3D information. Combining simultaneous 3D, single-shot, and ultrafast imaging makes LIF holography unique. Despite these advantages, digital LIF holography faces challenges in accurately modeling and reconstructing the recorded object due to the low coherence and spatiotemporal distortions [19–21]. This limits the ability of the technique to achieve high accuracy and precision, largely focusing on qualitative reconstructions. Because this is a signal processing problem, it could potentially be resolved with specialized algorithms. A major requirement is adapted algorithms to model ultrafast diffraction accurately and efficiently.

1.2. Contributions

Unfortunately, not many algorithmic solutions are available. Brute force simulations are too computationally expensive to be practical; this is already the case for conventional holography [22], but it is further exacerbated by including a time dimension. Recently, an FFT-based simulation was proposed designed for modeling numerical diffraction in LIF holography [18]; however, this model only accounts for particular LIF holography setup configurations, does not model the laser pulse shape, does not accurately account for the limited temporal coherence and does not model the hologram formation process for 3D objects. This limits the accuracy and applicability of the numerical simulation, potentially limiting understanding of the properties of the recorded sample and introducing distortions [23].

The present study alleviates these limitations by proposing a new algorithm for computing the LIF hologram formation process and reconstruction. Our specific contributions are as follows:

- We derive an analytical model extending the angular spectrum method (ASM) in time in the context of LIF holography.
- We propose an efficient convolutional approximation for the LIF hologram formation process in the frequency domain for any combination of reference and object pulse incidence angles.
- We give a theoretical analysis of the chosen algorithm parameters, including how to minimize the number of required samples.
- We generalize the temporal numerical diffraction framework to form LIF holograms of 3D objects.
- The algorithm is validated in numerical simulations and with a LIF holographic setup.

The remainder of this paper is organized as follows: Section 2 gives a detailed analytical derivation and algorithmic description of the newly proposed numerical diffraction model. In Section 3, we test the accuracy and efficiency of our models for multiple 2D and 3D objects and compare them with the reference technique. We finally conclude in Section 4.

2. Methodology

We introduce diffraction models for conventional (i.e., timeless) computer-generated holography (CGH). We then extend these models for rapidly time-varying signals and propose a compact 3D signal representation encoding the wavefront bot in space and time. This model is then applied for LIF holography, investigating the different cases $\theta_R = \theta_O$ and $\theta_R \neq \theta_O$, proposing a computationally efficient convolutional approach. We finally detail how to more accurately calculate the measured intensity on the recording device for LIF hologram formation.

2.1. Numerical diffraction for conventional holography

Starting from the expression for a point-spread function (PSF) in conventional holography, a point source with a complex-valued amplitude $a_j \in \mathbb{C}$ and spatial coordinates (x_j, y_j, z_j), which will create a complex-valued pattern P_j at the plane $z = 0$ given by

$$P_j(x, y; z) = \frac{a_j}{r_j} \exp\left(ikr_j\right) \quad \text{where} \quad r_j = \sqrt{(x - x_j)^2 + (y - y_j)^2 + (z - z_j)^2}. \tag{2}$$

where $k = 2\pi/\lambda$ is the wavenumber, λ is the wavelength and i is the imaginary unit.

We can calculate holograms of general objects and wavefronts using the Huygens-Fresnel diffraction model. This can be computed in CGH by discretizing objects (i.e., sampling) into a point cloud and summing over all point contributions, cf. Equation (2). That is, the wavefield U can be expressed as the sum of object points P_j, namely

$$U(x, y; z) = \sum_{j=1}^{M} P_j(x, y; z) = \sum_{j=1}^{M} \frac{a_j}{r_j} \exp\left(ikr_j\right) \tag{3}$$

However, this expression is computationally costly, as every hologram pixel needs to be updated for every object point. This can be calculated efficiently between parallel planes via a convolution, expressed through multipliers in Fourier space using the angular spectrum representation [24]:

$$\mathcal{A}(\omega, \eta; z) = \iint_{-\infty}^{+\infty} U(x, y; z) \exp\left(-i(z_2 - z_1)(x\omega + y\eta)\right) \mathrm{d}x\, \mathrm{d}y = \mathcal{F}_{2\mathrm{D}}\left\{U(x, y; z)\right\} \tag{4}$$

It decomposes a wavefront into plane waves through the two-dimensional (2D) Fourier transform $\mathcal{F}_{2\mathrm{D}}$. The angular spectrum of the wavefront at two different depth planes $z = z_1$ and $z = z_2$ are related by the expression

$$\mathcal{A}(\omega, \eta; z_2) = \mathcal{A}(\omega, \eta; z_1) \exp\left(-i(z_2 - z_1)\sqrt{k^2 - \omega^2 - \eta^2}\right). \tag{5}$$

This is called the “Angular spectrum method” (ASM), which can be used to propagate wavefronts over space efficiently. This model does not account for time variation, which we will tackle in the next section.

2.2. Extensions for rapidly time-varying signals

Consider the complex electric field of the form $E(x, y, t; z)$, assumed to be scalar and linearly polarized. We will extend the expressions from the previous section to include time.

We start by modeling the laser pulse over time rather than conventional continuous laser illumination. The shape of the laser pulse is typically characterized by its FWHM, denoted W_{th}. We model the pulse envelope as a Gaussian $\exp\left(-\left(\frac{t}{\tau}\right)^2\right)$ using the relationship $\tau = \frac{W_{\mathrm{th}}}{2\sqrt{\ln 2}}$. We express the laser pulse as

$$\Pi(t) = \Pi_0 \exp\left(ik_0ct - \left(\frac{t}{\tau}\right)^2\right) \tag{6}$$

where k_0 is the central frequency and Π_0 the laser pulse amplitude. The pulse peak is centered at $t = 0$ by convention. This can be represented in k-space via a Fourier transform

$$\hat{\Pi}(k) = \Pi_0 \tau \sqrt{\pi} \exp\left(-\frac{\tau^2 c^2}{4}(k - k_0)^2\right) = \hat{\Pi}_0 \exp\left(-\hat{\tau}^2(k - k_0)^2\right) \tag{7}$$

resulting again in a Gaussian offset by k_0, characterized by $\hat{\Pi}_0 = \Pi_0 \tau \sqrt{\pi}$ and $\hat{\tau} = \frac{\tau c}{2}$.

Suppose that we illuminate a 3D structure with that laser pulse. If we discretize it by a set of points, we can combine Eq. (3) and Eq. (6), giving us

$$E(x,y,t;z) = \sum_{j=1}^{M} \frac{a_j}{r_j} \exp\left(ik_0 \left(r_j + c(t-t_j) \right) - \left[\frac{t - t_j - c^{-1} r}{\tau} \right]^2 \right) \tag{8}$$

where t_j is the time offset when the light pulse peak reaches the point. The imaginary part of the expression in the exponential describes the wavefield oscillating over space (r_j) and time ($c(t-t_j)$). The real part of the expression describes the modulation by the laser pulse, cf. Equation (6), where the path length term is included ($c^{-1}r$) to account for the finite speed of light at these short timescales.

Representing the time-variant electric field at a certain z-plane now requires storing a 3D array parameterized by (x,y,t). Like in the previous case, every pixel over every time step must be updated by every point, making this expression computationally costly, especially because of the added time dimension. We thus intend to extend the ASM calculation method to account for time.

In free space, the scalar diffraction model is valid [24] §3.2. The ASM relies on the Helmholtz equation, which is a relation derived for purely monochromatic waves, cf. [24] §3.3.1. However, rapidly time-varying electromagnetic signals should be treated as polychromatic. Invoking the linearity of these models, it is possible to generalize nonmonochromatic wave propagation by treating polychromatic light as a linear superposition of monochromatic waves, integrating over a wavelength distribution [24] §3.8. There is theoretical support for this idea in [25] §5.1, using an angular spectrum representation of pulsed electromagnetic beams.

Given this reasoning, we extend the ASM over k-space, yielding

$$\mathcal{A}(\omega,\eta,k;z) = \iiint_{-\infty}^{+\infty} E(x,y,t;z) \exp\left(-i(x\omega + y\eta + tk)\right) \mathrm{d}x\, \mathrm{d}y\, \mathrm{d}t = \mathcal{F}_{3\mathrm{D}}\left\{E(x,y,t;z)\right\} \tag{9}$$

using the 3D Fourier transform $\mathcal{F}_{3\mathrm{D}}$, where the angular spectra are related by

$$\mathcal{A}(\omega,\eta,k;z_2) = \mathcal{A}(\omega,\eta,k;z_1) \exp\left(-i(z_2 - z_1)\sqrt{k^2 - \omega^2 - \eta^2}\right). \tag{10}$$

Straightforward discretization of the signal over the time dimension will not be computationally tractable. Consider tracking a signal modeled by a green laser pulse of $\lambda = 532$ nm with $W_{\mathrm{th}} = 200$ fs, propagating over $d = 10$ cm. Light needs about $d/c = 334$ ps to propagate over 10 cm, sampled to at least $\lambda/2c \approx 0.88$ fs, resulting in more than $3.8 \cdot 10^5$ time samples per pixel. Tracking all that data for millions of pixels would be impractical.

We can substantially reduce these requirements by leveraging that laser pulses are "sparse" in space, time, and k-space, i.e., the signals are only significant for certain wavelengths and specific regions in space and time. Since most of the signal is centered around k_0 in k-space, we demodulate the electric field by this carrier frequency, namely

$$U(x,y,t;z) = E(x,y,t;z) \cdot \exp(-ik_0ct). \tag{11}$$

This operation eliminates time dependence in conventional holography with an idealized monochromatic laser. Here, we obtain a low-pass signal characterized by the laser pulse bandwidth with a Gaussian envelope. We consider the bandwidth $K = 2\varsigma/\hat{\tau}$, where ς is the number of standard deviations where we treat the bandwidth as nonzero.

Furthermore, the time window in which the signal is significant at the object plane will typically be small compared to the time it takes for the light to propagate to a different plane. We can thus incorporate the time delay z/c needed for light to bridge the axial distance between two planes, which gives us, based on Eq. (10):

$$\begin{aligned} U\left(x, y, t + \frac{z}{c}; z\right) &= \mathcal{F}_{3\mathrm{D}}^{-1}\left\{\mathcal{F}_{3\mathrm{D}}\left\{U(x, y, t; 0)\right\} \exp\left(izk - iz\sqrt{k^2 - \omega^2 - \eta^2}\right)\right\} \\ &= \mathcal{F}_{3\mathrm{D}}^{-1}\left\{\mathcal{F}_{3\mathrm{D}}\left\{U(x, y, t; 0)\right\} \cdot \hat{\mathcal{K}}(\omega, \eta, k)\right\} \\ &= U(x, y, t; 0) * \mathcal{K}(x, y, t); \end{aligned} \tag{12}$$

namely, Eq. (12) can be expressed as a Fourier multiplier $\hat{\mathcal{K}}$ or equivalently as a convolution with the temporal ASM kernel $\mathcal{K}$. The number of needed samples N for a well-resolved discrete Fourier transform can be found by the following relations:

$$\Delta t = \frac{T}{N} = \frac{1}{K} \quad \text{and} \quad \Delta k = \frac{K}{N} = \frac{1}{T} \tag{13}$$

where Δt and Δk are the sampling step sizes in time and k-space, respectively; T is the considered time extent, and K is the bandwidth. If we use a time extent $T = 2$ ps and $\varsigma = 4$, the number of samples needed in the time dimension per hologram pixel for the previous example goes down to 44. This allows for the easier computational handling of ultrafast diffraction algorithms.

2.3. LIF holography configuration - general case

In LIF holography, we consider pulses that are incident under an angle θ w.r.t. the x-axis of the form

$$R_0 \exp\left(\left[\frac{t + x\sin\theta}{\tau}\right]^2\right) = R(t + \alpha x) \tag{14}$$

where $\alpha = \sin\theta$ is a constant setup parameter.

As shown in Fig. 1, the incidence angle for the reference pulse is θ_R and for the object pulse is θ_O, with corresponding constants $\alpha_R = \sin\theta_R$ and $\alpha_O = \sin\theta_O$. We model the object wavefront in the hologram plane H by

$$H(x, y, t + \alpha_R x) = O(x, y, t)R(t + \alpha_O x) * \mathcal{K}(x, y, t) \tag{15}$$

accounting for the time dependence of the measured wavefront along x because of the reference pulse. Using the coordinate transformation $t' = t + \alpha_R x$, we get

$$H(x, y, t') = O(x, y, t)R(t' + \alpha_O x - \alpha_R x) * \mathcal{K}(x, y, t' - \alpha_R x) \tag{16}$$

This expression is not an ordinary convolution anymore because of the dependence on x in the time coordinate of $\mathcal{K}$.

However, we can treat $\mathcal{K}$ as being *sheared*, for which we can find a mapping in Fourier space. Consider a 3D signal $S(x, y, t)$ and its Fourier transform $\hat{S}(x, y, t)$ which are related as follows

$$\hat{S}(\omega, \eta, k) = \mathcal{F}_{3\mathrm{D}}\left\{S(x, y, t)\right\} = \iiint_{-\infty}^{+\infty} S(x, y, t)e^{-i(x\omega + y\eta + tk)}\,\mathrm{d}x\,\mathrm{d}y\,\mathrm{d}t \tag{17}$$

If we shear the signal in the time dimension along x by s, we get

$$\begin{aligned} \mathcal{F}_{3\mathrm{D}}\left\{S(x, y, t - sx)\right\} &= \iiint_{-\infty}^{+\infty} S(x, y, t - sx)e^{-i(x\omega + y\eta + tk)}\,\mathrm{d}x\,\mathrm{d}y\,\mathrm{d}t \\ &= \iiint_{-\infty}^{+\infty} S(x, y, t - sx)e^{-i(x(\omega + sk) + y\eta + (t - sx)k)}\,\mathrm{d}x\,\mathrm{d}y\,\mathrm{d}t \\ &= \iiint_{-\infty}^{+\infty} S(x, y, u)e^{-i(x(\omega + sk) + y\eta + uk)}\,\mathrm{d}x\,\mathrm{d}y\,\mathrm{d}t \\ &= \hat{S}(\omega + sk, \eta, k) \end{aligned} \tag{18}$$

resulting in another shearing of the Fourier-domain signal, this time in the ω-dimension along k by $-s$. Thus, the Fourier transform of the wavefront at the hologram plane can be computed by

$$\hat{H}(\omega,\eta,k) = \mathcal{F}_{3\mathrm{D}}\left\{H(x,y,t')\right\} = \mathcal{F}_{3\mathrm{D}}\left\{O(x,y,t)R(t'+(\alpha_O-\alpha_R)x)\right\}\cdot\hat{\mathcal{K}}(\omega+\alpha_R k,\eta,k) \quad (19)$$

where $\hat{\mathcal{K}}$ is the temporal ASM kernel expressed in Fourier space as a multiplier.

The coherence between the signals will be maximal for $t'=0$, so we can approximate the found signal in the hologram plane by

$$H(x,y,t'=0) = \mathcal{F}_{2\mathrm{D}}^{-1}\left\{\int_{-\infty}^{+\infty}\hat{H}(\omega,\eta,k)\,\mathrm{d}k\right\}. \quad (20)$$

The latter will be more precise in Section 2.5. This proves that LIF holography cannot be modeled by a 2D convolution experimentally verified in [18]. We now have a general expression for any θ_R and θ_O.

2.4. Special case: equal incidence angles for illumination pulses

Prior works [18] showed that the special case $\alpha=\alpha_R=\alpha_O$ results in a 2D convolution. Thus, we can simplify the model further and allow for a direct comparison with the previous technique. We will show that this still holds in our newly proposed, more accurate model.

Continuing from Eq. (19), the α_R and α_O in R cancel out. Because of the separability of the Fourier transform, we get

$$\hat{H}(\omega,\eta,k) = \mathcal{F}_{2\mathrm{D}}\left\{O(x,y)\right\}\cdot\mathcal{F}_{1\mathrm{D}}\left\{R(t)\right\}\cdot\hat{\mathcal{K}}(\omega+\alpha k,\eta,k) = \hat{O}(\omega,\eta)\hat{R}(k)\hat{\mathcal{K}}(\omega+\alpha k,\eta,k). \quad (21)$$

We would like to find an analytical expression for the 2D convolution kernel, found by integrating over the time dimensions as done in Eq. (20), giving

$$\mathcal{F}_{2\mathrm{D}}\left\{H(x,y,t'=0)\right\} = \int_{-\infty}^{+\infty}\hat{H}(\omega,\eta,k)\,\mathrm{d}k = \hat{O}(\omega,\eta)\int_{-\infty}^{+\infty}\hat{R}(k)\hat{\mathcal{K}}(\omega+\alpha k,\eta,k)\,\mathrm{d}k \quad (22)$$

This expression does not seem to have a closed-form analytical solution. Nonetheless, the expression will only be significant near k_0 since it is multiplied by $\hat{R}(k)$ which is a Gaussian centered around k_0. We, therefore, take the Taylor expansion of the expression within the exponential of $\hat{\mathcal{K}}$ (cf. Equation (12)), yielding a quadratic approximation

$$\sqrt{k^2-(\omega+\alpha k)^2-\eta^2}-k = \rho-k_0+(\chi-1)(k+k_0)+\frac{1-\alpha^2-\chi^2}{2\rho^2}(k+k_0)^2+O\left((k+k_0)^3\right) \quad (23)$$

where $\rho=\sqrt{k_0^2-\omega^2-(\eta+\alpha k_0)^2}$, and $\chi=\frac{k_0(1-\alpha^2)-\alpha\omega}{\rho}$.

This means that the expression in the integral Eq. (22) can be written in the form

$$\hat{R}(k)\hat{\mathcal{K}}(\omega+\alpha k,\eta,k)\approx\exp\left(ak^2+bk+c\right) \quad (24)$$

where $a,b,c\in\mathbb{C}$ are complex-valued expressions independent of k. This has an analytical solution:

$$\int_{-\infty}^{+\infty}\exp\left(ak^2+bk+c\right)\mathrm{d}k = \sqrt{\frac{\pi}{-a}}\exp\left(c-\frac{b^2}{4a}\right) \quad (25)$$

which holds for any complex-valued $a,b,c\in\mathbb{C}$ so long as the real part $\Re(a)<0$.

We can now find the spectrum of the signal at the hologram plane with

$$\int_{-\infty}^{+\infty}\hat{H}(\omega,\eta,k)\,\mathrm{d}k = \hat{O}(\omega,\eta)\cdot\sqrt{\pi\xi}\exp\left(iz(\rho-k_0)+\frac{z^2\xi}{4}(\chi-1)^2\right) \quad (26)$$

where $\xi=\frac{2\rho}{iz(\alpha^2+\chi^2-1)-2\rho\tau^{-2}}$. Using the inverse 2D Fourier transform, we can retrieve the signal in the hologram efficiently from Eq. (26).

2.5. Accurate intensity modeling

The reference method [18] used an approximate condition to determine whether interference occurred based on the inequality Eq. (1), also without accounting for the time dependence of the reference pulse. We will use a more accurate model.

Digital cameras can only measure the intensity of light accumulated over time. To further increase the accuracy, we model the intensity I of the signal by

$$I = \int_{-\infty}^{+\infty} |R(t) + O(t)|^2 dt \tag{27}$$

where we consider the camera integration time to be infinite compared to the ultrashort laser pulse time. Parseval's equality relates a signal $S(t)$ and its Fourier transform $\hat{S}(k)$ with

$$\int_{-\infty}^{+\infty} |S(t)|^2 dt = \int_{-\infty}^{+\infty} |\hat{S}(k)|^2 dk \tag{28}$$

so that we can find analytical expressions for whichever transform space is more convenient. Thus, we can skip the inverse Fourier transform along the time dimension when calculating the resulting intensity.

3. Experiments

This section will first evaluate the special case where the reference (θ_R) and object (θ_O) pulse incidence angles are equal, which can be expressed as a 2D convolution. We experimentally verify the technique with a LIF hologram acquired in an optical setup using a visual comparison. We compare it with the previous reference method [18] quantitatively and qualitatively. Then, we show that our approach can also compute the general case $\theta_R \neq \theta_O$ efficiently, unlike earlier approaches in the state-of-the-art. Finally, we show the flexibility of the technique to model 3D objects, as prior techniques have limited themselves to 2D apertures.

3.1. LIF hologram: special case $\theta_R = \theta_O$

We briefly introduce the reference technique based on [18] here; the convolution kernel h_{LIF} for the case $\theta_R = \theta_O$ is expressed in the spatial domain, essentially consisting of a masked PSF:

$$h_{\text{LIF}} = \begin{cases} \frac{z}{i\lambda r^2} \exp\left(i\frac{2\pi}{\lambda} r\right) & \text{if } |\alpha x + z - r| < cW_{\text{th}} \ \wedge \ \max(x,y) < \frac{|z|\lambda}{\sqrt{4p^2 - \lambda^2}} \\ 0 & \text{otherwise.} \end{cases} \tag{29}$$

In other words, the PSF is only evaluated if it satisfies (1) the LIF path length condition and (2) the aliasing condition. The second condition was not used in the original work but was included here for correctness when z gets smaller; otherwise, it will lead to aliasing because the finite sampling pitch may be lower than the PSF frequency at high radii; the condition corresponds to the "circumscribed square" case from [26].

For the first experiment, we compare the PSF for a simulated LIF hologram where $\theta = \theta_R = \theta_O = 10°$, $W_{\text{th}} = 200$ fs, pixel pitch $p = 5$ µm, $\lambda = 532$ nm and $z = 45$ mm. Three methods are compared in Fig. 2: (a) the reference method using Eq. (29), (b) the proposed LIF holography expression integrated over time as in Eq. (20), and (c) the special case model derived in Eq. (26).

We used the generated signals' peak signal-to-noise ratio (PSNR) to evaluate the differences quantitatively. The PSNR between the proposed general and approximated models (b and c) is 91.0 dB, showing the high accuracy of the approximation. They are visually indistinguishable, explained by the normalized error map shown in Fig. 3, which goes only up to $5.5 \cdot 10^{-11}$. The PSNR of the reference method (a) with either proposed method is 44.0 dB, as the error is much larger. The impact will be shown in the following experiment.

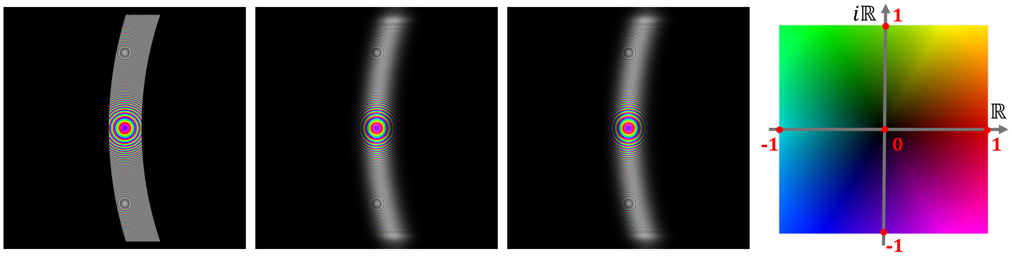

(a) Reference method (b) Proposed (general case) (c) Proposed (special case) (d) Color scale

Fig. 2. Side-by-side comparison of different PSFs calculated by (a) the reference method, (b) the proposed method valid in the general case, and (c) the approximated special case. (d) The PSFs are color-coded using a normalized scale with brightness for magnitude and hue for phase.

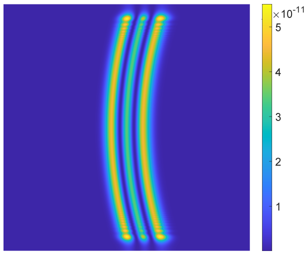

Fig. 3. Normalized squared error map, with associated color scale, comparing the general case model from Fig. 2(b) with the special case model from Fig. 2(c).

We used data from an experimental LIF holography setup for the qualitative experiment as explained in [18]. This optical setup involved a mode-locked ultrashort pulsed laser (Spectra-Physics Inc., "HighQ-2 SHG") with a central wavelength of $\lambda = 522$ nm and $W_{\text{th}} = 200$ fs. The light pulse from the laser is passed through a beam splitter and transmitted to a diffuser plate. A 17 mm × 17 mm 1951 USAF resolution test chart is set on the diffuser plate to help recognize temporal changes in the light pulse. The image sensor has a 2592 × 1944 pixel resolution and a pixel pitch of $p = 2.2$ µm.

The acquisitions are compared to a simulation with the reference and proposed methods. Using identical settings to the experimental setup for all parameters, 2592 × 1944 pixel holograms were computed, superimposing the propagated object wavefront with the reference wavefront as explained in Section 2.5.

For the three holograms, moving pictures were reconstructed according to the same process: we set the resolution of each sub-hologram to 512 × 1944 pixels, moving the window by steps of 32 pixels along the x-axis, resulting in 66 frames with a temporal interval of ~8.2 fs. We then applied bandpass-filtered the holograms to eliminate the zeroth-order diffraction and twin image, followed by an ASM backpropagation operation. A selection of the frames are shown in Fig. 4.

We observe the object's light pulse propagating from left to right over time, as evidenced by the changing pattern of the test chart in each image, consistent with experimental results demonstrated in prior work [17]. The agreement between the simulation results and the experimental behavior of the object light pulse validates the proposed method. Note that while the edges of the reconstructed images in the simulations for the reference were sharp, they appear blurred in the proposed method thanks to using a Gaussian pulse model, matching the experimental results. There is still some visible difference between the pulse envelope shape of the reference recording

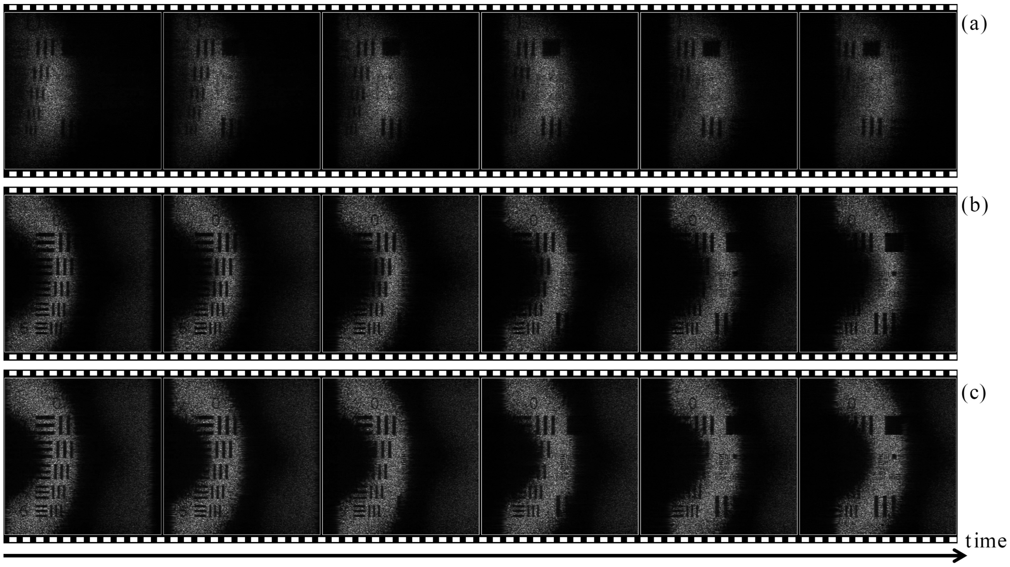

Fig. 4. Moving pictures of a propagating light pulse over a USAF pattern for (a) the hologram recorded in the experimental setup and the holograms calculated in the (b) proposed and (c) reference methods, respectively. Here, a small selection of frames separated by ~90 fs from the video is shown.

and the proposed method in Fig. 4. This could be due to differences in how the first-order component is filtered from the off-axis hologram, non-ideal imaging components in the optical setup, or remaining approximations in the proposed propagation algorithm.

3.2. LIF hologram: general case

We now consider the general case $\theta_R \neq \theta_O$. Note that the reference method [18] cannot be used here anymore since the propagation operator cannot be written as a 2D convolution. This was demonstrated experimentally [18], meaning that acceleration was only possible for the special case $\theta_R = \theta_O$. The effect is also shown in Fig. 5, showing the PSF for impulses in the object plane set at different lateral positions. For a convolution to be possible, the PSF should be translation-invariant.

In our more general model, we can express the numerical diffraction of a wavefront where $\theta_R \neq \theta_O$ as a *3D convolution* via Eq. (19). This means that we can still model diffraction efficiently for all LIF holography setup configurations.

In our numerical experiments, we calculated the wavefront of a USAF resolution test chart aperture (cf. Figure 6) on a diffuser plate modeled with random phase. The simulation parameters were set to $\theta_R = 6°$, $\theta_O = 4°$, $W_{\text{th}} = 200$ fs, $p = 5$ µm, $\lambda = 532$ nm, $z = 5$ cm and $\varsigma = 4$. We implemented the proposed algorithm on GPU and compared it to the full calculation method. We used a machine with an AMD Ryzen Threadripper PRO 5995WX CPU, 256 GB RAM, NVIDIA RTX A6000 GPU and a Windows 11 OS. The code was implemented in MATLAB using 32-bit floating point precision.

The calculation time results are reported in Table 1, showing over 4 orders of magnitude speed gains over the reference full calculation method. Please note that the speed-up magnitude may differ in a fully optimized C++/CUDA implementation since MATLAB is an interpreted language where different functions and libraries are not optimized to the same degree.

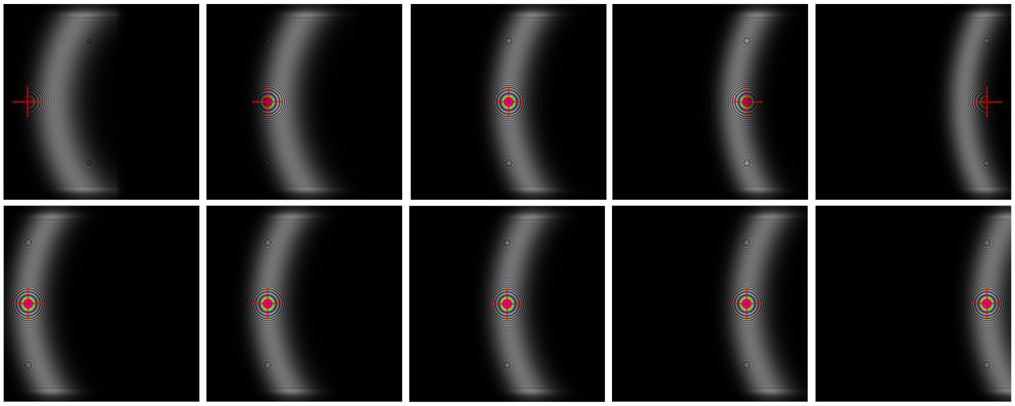

Fig. 5. Computed PSFs for different impulse positions and values of θ_R and θ_O. The upper row shows PSFs for $\theta_R = 6°$ and $\theta_O = 4°$; the bottom row ones where $\theta_R = \theta_O = 6°$. PSFs are shown for impulses horizontally sampled at positions separated by ~1 mm from left to right. The images are color-coded using brightness for magnitude and hue for phase, using the same color scale as in Fig. 2(d). The red marker crossed indicates the center of the corresponding conventional time-less PSF, cf. Equation (2). Note how the response is only translation-invariant for the case $\theta_R = \theta_O$; the other case's amplitude support and frequency content are variable.

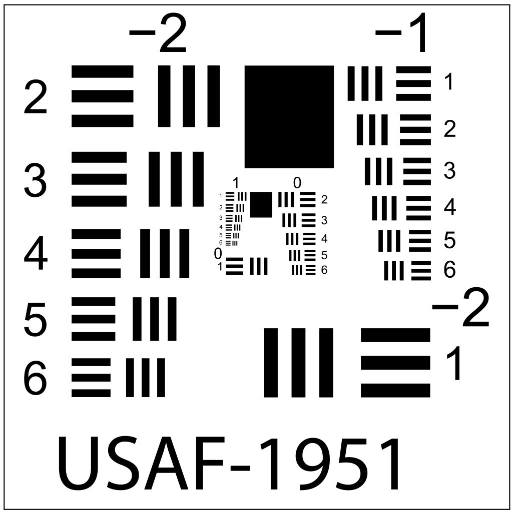

Fig. 6. USAF test chart pattern used in the numerical experiments.

Table 1. Comparison of calculation times between the full calculation and the proposed method. The proposed method's calculation times are averaged over 1000 runs.

resolution	full calculation (s)	proposed method (s)	speed-up (ratio)
512×512	117.0	0.00250	$4.69 \cdot 10^4$
1024×1024	511.1	0.00911	$5.61 \cdot 10^4$
2048×2048	3139.0	0.370	$8.53 \cdot 10^4$

3.3. LIF hologram of a 3D object

Besides modeling general LIF holography configurations, the newly proposed model also lends itself to efficiently modeling the diffraction of light on 3D objects, unlike previous algorithms, which only worked with flat objects parallel to the hologram plane. Our approach is inspired by multiplane CGH [27,28], partitioning the scene axially into layers, processing, and propagating the wavefront layer by layer from back to front. We will extend this principle by including the time component.

Consider a reflective surface with a depth profile $D[x, y] \in [z_{\min}, z_{\max}]$ along z whose reflectance is given by $A[x, y]$; the test object is shown on Fig. 7. If we use N layers, we can model propagation between subsequent layers as a propagation with a short distance of $\Delta z = \frac{N}{z_{\max} - z_{\min}}$. For efficiency, we can precompute and reuse the temporal ASM propagation kernel $\mathcal{K}_{\Delta z}$ for every layer.

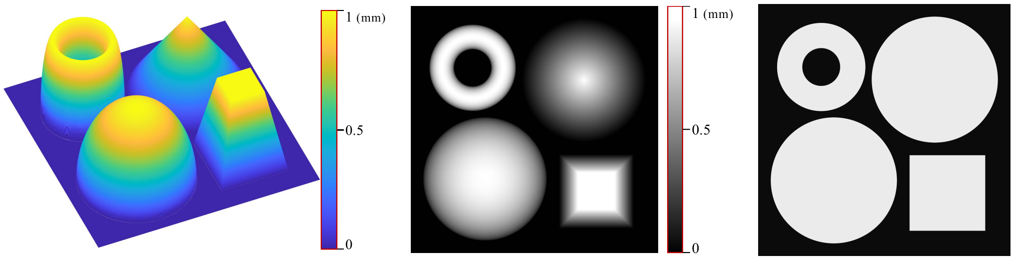

(a) 3D model (b) Height map $D[x, y]$ (c) Reflectance map $A[x, y]$

Fig. 7. Diagrams showing the attributes of the 3D test model.

We define the masked amplitude $M_j[x, y]$ as the reflectance sectioned by depth in each layer indexed by $j \in \{0, 1, \dots, N-1\}$:

$$M_j[x, y] = \begin{cases} A[x, y] & z_{\min} + j\Delta z \leq D[x, y] < z_{\min} + (j+1)\Delta z \\ 0 & \text{otherwise.} \end{cases} \tag{30}$$

We propagate the temporal wavefield U_j successively for each j, starting at $j = 0$ with $U_0(x, y, t) = M_0[x, y]R(t)$. Each subsequent layer is calculated using the previous one, where we get for $j \geq 1$:

$$U_j(x, y, t) = U_{j-1}(x, y, t) * \mathcal{K}_{\Delta z} + M_j[x, y]R\left(t - \frac{j\Delta z}{c}\right). \tag{31}$$

Note that we use a different time delay as an argument for the reference beam R at each layer since the incoming reference beam will need less time to reach object positions closer to the light source. Finally, when the object has been fully processed, we use a final temporal ASM propagation with a larger distance d to reach the hologram plane. Figure 8 summarizes this process.

The moving pictures were reconstructed using the same process as the one used in Section 3.1. Each sub-hologram had dimensions of 512 × 2048 pixels, with a moving window of 8 pixels along the x-axis, resulting in 193 frames with a temporal interval of ~18 fs. A selection of the frames is shown in Fig. 9. See Visualization 1 for the original video source material. We can observe a sectioning of the object, where the front of the object closest to the camera will appear first, progressively revealing deeper parts of the object's surface. This validates the 3D version of our ultrafast diffraction algorithm for LIF holography.

Optionally, occlusion can also be modeled in the progressing wavefront by blocking light from preceding layers at sliced object positions as done in [28]. This could even enable modeling more complex volume structures that are not representable by a single depth map.

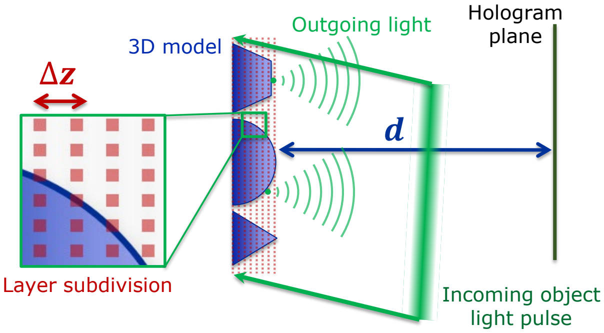

Fig. 8. Diagram of the 3D sample illumination scheme for the part of the setup that is illuminated by the object pulse. The incoming object pulse is a plane wave temporally modulated by the pulse amplitude, where the reflection time delay in each sample point is dependent on the sample depth. The 3D object is subdivided into layers, using the newly proposed temporal ASM successively for each layer over a distance of Δz. Finally, the last layer is propagated to the hologram plane by a larger distance d, interfering with the reference pulse (not shown) and forming the final detected interference pattern.

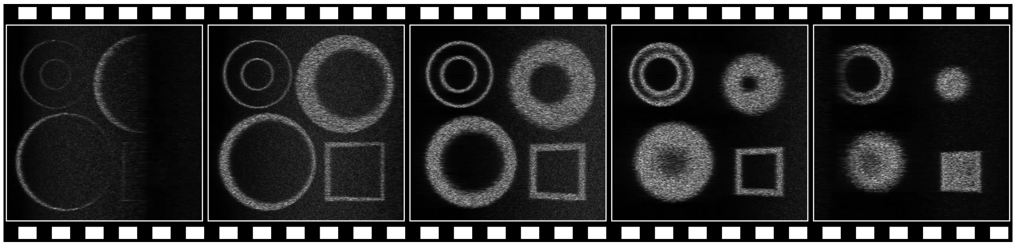

Fig. 9. Moving pictures of a propagating light pulse reflecting on a 3D surface. The object's shape can be seen thanks to the different light path lengths from the object's surface. A small selection of frames separated by ~800 fs from Visualization 1 is shown.

4. Conclusion

Digital LIF holography is a unique ultrafast imaging technique capable of fully encoding and reconstructing the wavefield of light in a single shot. However, digital LIF holography faces challenges in accurately modeling and reconstructing the recorded object despite these advantages because of low coherence and spatiotemporal distortions. We propose novel algorithms for modeling ultrafast diffraction in LIF holography, demonstrating (1) improved accuracy, (2) efficient modeling of the LIF hologram formation processing for arbitrary configurations of the tilt angles, resulting in 4 to 5 orders of magnitude speed-up, and (3) a newly proposed algorithm for imaging 3D objects. We hope that this work contributes to higher-precision ultra-fast imaging of various samples in digital LIF holography. Future work will involve testing the accuracy and applicability of the proposed propagation technique, which should involve a highly precise experimental reference technique for validation. Moreover, future work will investigate more complex samples, model additional light-material interactions (such as scattering, specular reflections, transparency, etc.), and use computational techniques to reduce spatiotemporal distortions further.

Funding. Japan Society for the Promotion of Science (20H05887, 23KF0011, International Research Fellow P22752); Fonds Wetenschappelijk Onderzoek (12ZQ223N, G0A3O24N).

Disclosures. The authors declare no conflicts of interest.

Data availability. Data underlying the results presented in this paper are not publicly available at this time but may be obtained from the authors upon reasonable request.

References

1. T. Inoue, T. Kakue, K. Nishio, *et al.*, "Recent advances in imaging of light propagation with light-in-flight recording by holography," Ultrafast Sci. **3**, 0043 (2023).
2. T. Inoue, T. Aoyama, Y. Sawashima, *et al.*, "Motion picture of magnified light pulse propagation with extending recordable time of digital light-in-flight holography," Appl. Opt. **61**(5), B206–B214 (2022).
3. A. Ehn, J. Bood, Z. Li, *et al.*, "Frame: femtosecond videography for atomic and molecular dynamics," Light: Sci. Appl. **6**(9), e17045 (2017).
4. R. Osellame, H. J. Hoekstra, G. Cerullo, *et al.*, "Femtosecond laser microstructuring: an enabling tool for optofluidic lab-on-chips," Laser Photonics Rev. **5**(3), 442–463 (2011).
5. R. Hillenbrand, T. Taubner, and F. Keilmann, "Phonon-enhanced light–matter interaction at the nanometre scale," Nature **418**(6894), 159–162 (2002).
6. D. Zhang, Q. Gao, B. Li, *et al.*, "Femtosecond laser-induced plasma spectroscopy for combustion diagnostics in premixed ammonia/air flames," Appl. Opt. **58**(28), 7810–7816 (2019).
7. T. G. Etoh, T. Okinaka, Y. Takano, *et al.*, "Light-in-flight imaging by a silicon image sensor: Toward the theoretical highest frame rate," Sensors **19**(10), 2247 (2019).
8. X. Wang, L. Yan, J. Si, *et al.*, "High-frame-rate observation of single femtosecond laser pulse propagation in fused silica using an echelon and optical polarigraphy technique," Appl. Opt. **53**(36), 8395–8399 (2014).
9. S. Heuke, X. Audier, and H. Rigneault, "Double-modulation stimulated raman scattering: how to image up to 16-fold faster," Opt. Lett. **48**(2), 423–426 (2023).
10. L. Gao, J. Liang, C. Li, *et al.*, "Single-shot compressed ultrafast photography at one hundred billion frames per second," Nature **516**(7529), 74–77 (2014).
11. P. Wang and L. V. Wang, "Single-shot reconfigurable femtosecond imaging of ultrafast optical dynamics," Adv. Sci. **10**(13), 2207222 (2023).
12. D. Staselko, Y. N. Denisyuk, and A. Smirnov, "Holographic recording of the time-coherence pattern of a wave train from a pulsed laser source," Opt. Spectrosc. **26**, 225 (1969).
13. N. Abramson, "Light-in-flight recording by holography," Opt. Lett. **3**(4), 121–123 (1978).
14. N. H. Abramson and K. G. Spears, "Single pulse light-in-flight recording by holography," Appl. Opt. **28**(10), 1834–1841 (1989).
15. H. Hinrichs, K. D. Hinsch, J. Kickstein, *et al.*, "Light-in-flight holography for visualization and velocimetry in three-dimensional flows," Opt. Lett. **22**(11), 828–830 (1997).
16. B. Nilsson and T. E. Carlsson, "Direct three-dimensional shape measurement by digital light-in-flight holography," Appl. Opt. **37**(34), 7954–7959 (1998).
17. T. Kakue, K. Tosa, J. Yuasa, *et al.*, "Digital light-in-flight recording by holography by use of a femtosecond pulsed laser," IEEE J. Sel. Top. Quantum Electron. **18**(1), 479–485 (2012).
18. T. Kakue, T. Inoue, T. Shimobaba, *et al.*, "FFT-based simulation of the hologram-recording process for light-in-flight recording by holography," J. Opt. Soc. Am. A **39**(2), A7–A14 (2022).
19. N. Abramson, "Time reconstructions in light-in-flight recording by holography," Appl. Opt. **30**(10), 1242–1252 (1991).
20. A. Komatsu, Y. Awatsuji, and T. Kubota, "Dependence of reconstructed image characteristics on the observation condition in light-in-flight recording by holography," J. Opt. Soc. Am. A **22**(8), 1678–1682 (2005).
21. T. Inoue, M. Sasaki, K. Nishio, *et al.*, "Influence of the lateral size of a hologram on the reconstructed image in digital light-in-flight recording by holography," Appl. Opt. **60**(10), B59–B64 (2021).
22. D. Blinder, T. Birnbaum, T. Ito, *et al.*, "The state-of-the-art in computer generated holography for 3d display," Light: Adv. Manufact. **3**(3), 1 (2022).
23. D. Blinder and T. Kakue, "Numerical models for ultrafast diffraction in light-in-flight holography," in *Information Photonics, Optics & Photonics International Congress 2024*, Yokohama, Japan, (2024), pp. IP7–01.
24. J. W. Goodman, *Introduction to Fourier Optics - 4th edition* (W. H. Freeman and Company, 2017).
25. J. A. Marozas, "Angular spectrum representation of ultrawideband electromagnetic pulse propagation in lossy, dispersive dielectric slab waveguides," Ph.D. thesis, Citeseer (1998).
26. D. Blinder, T. Birnbaum, and P. Schelkens, "Pincushion point-spread function for computer-generated holography," Opt. Lett. **47**(8), 2077–2080 (2022).
27. N. Okada, T. Shimobaba, Y. Ichihashi, *et al.*, "Band-limited double-step fresnel diffraction and its application to computer-generated holograms," Opt. Express **21**(7), 9192–9197 (2013).
28. A. Symeonidou, D. Blinder, A. Munteanu, *et al.*, "Computer-generated holograms by multiple wavefront recording plane method with occlusion culling," Opt. Express **23**(17), 22149–22161 (2015).